Electronic Supplementary Material (ESI) for Energy & Environmental Science.
This journal is © The Royal Society of Chemistry 2014

Electronic Supplementary Information

Functional Graphene Nanomesh Foam

Yang Zhao,[a] Chuangang Hu,[a] Long Song,[a] Lixia Wang,[a] Gaoquan Shi,[b] Liming Dai,[c] and Liangti Qu*[a]

[a] Key Laboratory of Cluster Science, Ministry of Education of China, Beijing Key Laboratory of Photoelectronic/Electrophotonic Conversion Materials, Department of Chemistry, School of Science, Beijing Institute of Technology, Beijing 100081, P. R. China.

[b] Department of Chemistry, Tsinghua University, Beijing 100084, P. R. China.

[c] Department of Macromolecular Science and Engineering, Case School of Engineering, Case Western Reserve University, 10900 Euclid Avenue, Cleveland, Ohio 44106, United States.

* E-mail: lqu@bit.edu.cn

Experimental

Preparation of the N-doped graphene nanomesh foam (N-GMF) : Graphene oxide (GO) was prepared by oxidation of the natural graphite powder using a modified Hummers method as reported in our previous paper.[s1] For preparation of the N-GMF, 30 mL homogeneous GO (1 mg/mL) and 3 vol% pyrrole (Py) aqueous dispersion was pre-mixed and sealed in a 50mL Teflon-lined autoclave and maintained at 180 °C for 6h. After the autoclave was naturally cooled down to room temperature, the prepared gel was immersed into 40ml $FeCl_3$ (10g/250ml) for 1h. After heating the freeze-dried graphene gel at 850°C for 2h with a heating speed of 5 °C/min under Ar atmosphere, the N-GMF was obtained by removing the Fe_2O_3 with 8M HCl and washing the residue until pH is equal to 7.0. Here, $FeCl_3$ acts not only as the oxidant for polymerization of pyrrole, but also as the precursor of Fe_2O_3 nanoparticles, which can be the nucleation sites for site-localized etching of graphene.

Preparation of the S-doped GMF (S-GMF): For preparation of the S-GMF, 30 mL homogeneous GO (1 mg/mL) was sealed in a 50mL Teflon-lined autoclave and maintained at 180 °C for 6h. The prepared gel was immersed into 40ml $FeCl_3$ (10g/250ml) for 1h, followed by freeze drying. After heating the freeze-dried graphene gel and sulfur powder (weight 1:1) at 850 °C for 2h with a heating speed of 5 °C/min under Ar atmosphere, the S-GMF was obtained by removing the Fe_2O_3 using 8M HCl and washing the residue until pH=7.0.

Preparation of the N-S-codoped GMF (N-S-GMF): The N-S-GMF was prepared by heating the freeze-dried gel precursor of the N-GMF with sulfur powder (weight 1:1) at 850°C for 2h with a heating speed of 5 °C/min under Ar atmosphere, the N-S-GMF was obtained by removing the Fe_2O_3 with 8M HCl and washing the residue until pH=7.0.

Preparation of GMF: For preparation of the GMF, 30 mL homogeneous GO (1 mg/mL) was sealed in a 50mL Teflon-lined autoclave and maintained at 180 °C for 6h. The prepared gel was immersed into the 40 ml $FeCl_3$ (10g/250ml) for 1h and then freeze dried. After heating the freeze-dried graphene gel at 850 °C for 2h with a heating speed of 5 °C/min under

Ar atmosphere, the GMF was obtained by removing the Fe_2O_3 with 8M HCl and washing the residue until pH=7.0.

Preparation of other compared catalysts

Pure graphene foam (GF): For preparation of the pure G foam, 30 mL homogeneous GO (1 mg/mL) aqueous dispersion was sealed in a 50mL Teflon-lined autoclave and maintained at 180 ^{o}C for 6h. Then the freeze-dried graphene gel was annealed at 850^{o}C for 2h with a heating speed of 5 ^{o}C/min under Ar atmosphere.

N-doped graphene foam (N-GF): For the N-GF, 30 mL homogeneous GO (1 mg/mL) and 3 vol% pyrrole (Py) aqueous dispersion was pre-mixed and sealed in a 50mL Teflon-lined autoclave and maintained at 180 ^{o}C for 6h. Then the graphene/Py gel was immersed into the 40ml $FeCl_3$ (10g/250ml) for 1h and washed with water to remove the residue $FeCl_3$. Then N-GF was obtained after annealling the freeze-dried graphene gel at 850^{o}C for 2h with a heating speed of 5 ^{o}C/min with Ar atmosphere.

The S-doped graphene foam (S-GF): For S-GF, 30 mL homogeneous GO (1 mg/mL) aqueous dispersion was sealed in a 50mL Teflon-lined autoclave and maintained at 180 ^{o}C for 6h. The S-GF was synthetised after annealing the freeze-dried graphene gel and sulfur powder (weight 1:1) at 850 ^{o}C for 2h with a heating speed of 5 ^{o}C/min under Ar atmosphere.

The N-S-codoped graphene foam (N-S-GF): For the N-S-GF, 30 mL homogeneous GO (1 mg/mL) and 3 vol% pyrrole (Py) aqueous dispersion was pre-mixed and sealed in a 50 mL Teflon-lined autoclave and maintained at 180 ^{o}C for 6h. After heating the freeze-dried graphene gel and sulfur powder (weight 1:1) at 850^{o}C for 2h with a heating speed of 5 ^{o}C/min under Ar atmosphere, the N-S-GF was obtained.

Preparation of the sulfur doped Vulcan Carbon (S-Vulcan Carbon): The S-Vulcan Carbon was produced by mixing Vulcan carbon and sulfur powder (weight 1:1) together and then treating it at 850 ^{o}C for 2h with a heating speed of 5 ^{o}C/min under Ar atmosphere.

Electrochemical measurement: Cyclic voltammetry (CV) behavior of the N-GMF, GF and N-GF electrodes were investigated on CHI660D electrochemical workstation in three-electrode systems. 2mg of the samples were dispersed in 0.5ml ethanol and then was ultrasonicated to obtain a homogenous catalyst ink. 4μl of the ink was dipped on a glass carbon electrode (GC,*ca.* 0.196 cm^2) with 1μl of Nafion solution (5%) and dried in air. The mass loading is 0.081 mg/cm^2. 0.1 M PBS solution containing 0.1 M KCl solution was used as electrolyte. The potential range for CV test was -0.1– 0.5V. The scan rate for CV is 50mV/s.

For NH_3 sensing test, the samples (1.5mm×4mm×1.5mm) with the mass of 0.04mg were placed on a chip glass carrier (1cm×2cm) with both sides being attached by conductive silver epoxy and then directly connected to the current collector by two-electrode system.

Oxygen reduction reaction (ORR) measurement: The 2mg N-S-GMF was first ultrasonically dispersed in 0.5ml ethanol with 50μl of Nafion solution (5%), then the mixed suspensions (~5μl) were attached onto a glass carbon (GC) electrode (*ca.* 0.25 cm^2) as working electrode with the mass loading of 0.080 mg/cm^2, although the perpared catalysts can also be directly adhered on the GC electrode for testing (Figure S31). Measurements on a rotating ring-disk electrode (RRDE) and/or rotating disk electrode (RDE) were carried out on a MSRX electrode rotator (Pine Instrument) and the CHI 760D potentiostat. 0.1 M KOH was used as the electrolyte. A Pt wire and Ag/AgCl were used as counter and reference electrodes, respectively. The commercial Pt/C catalyst (20wt% platinum on carbon black) with the similar amount (~20μg) was also studied for comparison. N_2 or O_2 was used to give the O_2-free or O_2-saturated electrolyte solution.

The transferred electron number (n) per O_2 molecule involved in ORR was calculated from Koutecky-Levich equation. The current density j is related to the rotation rate ω of the electrode according to

$$1/j=1/j_k+1/B\omega^{0.5} \qquad \text{(S1)}$$

where j_k is the kinetic current and B is Levich slope which is given by

$$B=0.2nF(D_{O2})^{2/3}v^{-1/6}C_{O2} \qquad \text{(S2)}$$

Here n is the number of electrons transferred in the reduction of one O_2 molecule, F is the Faraday constant (F = 96485 C mol^{-1}), D_{O2} is the diffusion coefficient of O_2 in 0.1M KOH (D_{O2} =1.9 ×10^{-5} cm^2 s^{-1}), v is the kinematics viscosity (v = 0.01 cm^2 s^{-1}) and C_{O2} is concentration of O_2 in the solution (D_{O2} = 1.2 × 10^{-6} mol cm^{-3}). The constant 0.2 is adopted when the rotation speed is expressed in rpm.

The n was also determined from the RRDE measurement.

$$n = 4I_d/(I_d+I_r/N) \qquad \text{(S3)}$$

The peroxide percentage (% HO_2^-) was calculated based on the equation:

$$\%HO_2^-=200\times I_r/N/(I_d+I_r/N) \qquad \text{(S4)}$$

Here I_d and I_r is the disk current and ring current, respectively, and N is the current collection efficiency of Pt ring and determined to be 0.37.

Characterization: The morphology of the prepared samples was investigated by scanning (SEM, JSM-7500F) and transmission (TEM, 7650B, Hitachi) electron microscopy. The elemental mappings were performed on a scanning transmission electron microscope (STEM) unit with high-angle annular dark-field (HAADF) detector (HITACHI S-5500) operating at 30 kV. X-ray diffraction (XRD) patterns were obtained by using a Netherlands 1710 diffractometer with a Cu Kα irradiation source (λ = 1.54 Å), and a self-calibration process was performed with a SiO_2 internal standard sample prior to target measurement. Raman spectra were recorded using a RM 2000 Microscopic Confocal Raman Spectrometer

(Renishaw PLC, England) with a 514.5 nm laser. Nitrogen adsorption experiments were conducted at 77K using a TriStarII3020 (Micromeritics Instrument Corporation) apparatus. Before adsorption measurements, the samples were degassed in vacuum at 473K for 4h. The Pore size distribution and the specific surface areas (SSAs) of the samples were obtained by Barrett–Joyner–Halenda (BJH) and Brunauer Emmett Teller (BET) analyses of their adsorption isotherms. X-ray photoelectron spectroscopy (XPS) data were obtained with an ESCALab220i-XL electron spectrometer from VG Scientific using 300W AlKα radiation.

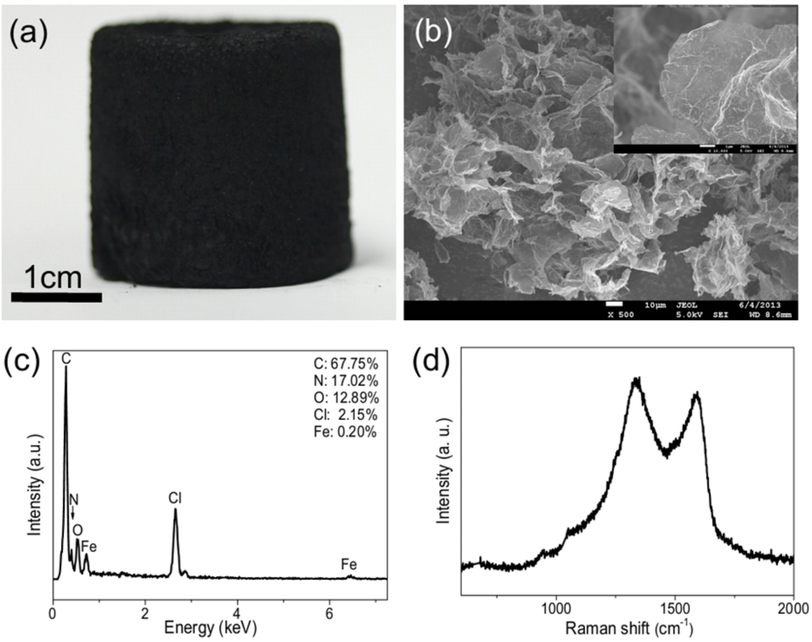

Figure S1. (a) The photo and (b) SEM images of the PPy/graphene@$FeCl_3$ foam after freeze drying and (c) the corresponding energy-dispersive spectrometry (EDS) spectrum of (a). (d) Raman spectra of PPy/graphene@$FeCl_3$ foam. Scale bar: b, 10μm; b inset, 1 μm.

The characteristics of PPy/graphene@$FeCl_3$ foam are shown in Figure S1a and b. From the energy-dispersive spectrometry (EDS) spectrum (Figure S1c), the low oxygen content and much high Cl content of PPy/graphene@$FeCl_3$ foam indicated that there was almost no any hydrolysis happened during immersing into the $FeCl_3$ solution for1h. The appearance of nitrogen element with much high content is from the polypyrrole (PPy), which is confirmed by the Raman spectrum shown in Figure S1d. After immersed into the oxidant aqueous $FeCl_3$solution, the PPy/graphene@$FeCl_3$ foam exhibits two obvious typical bands indexed at ~1334 and ~1597 cm^{-1} attributed to the D and G bands of hydrothermally graphene which are almost cover the peaks of the PPy (centered at 1238, 1370, 1410 and 1597 cm^{-1}), only leaving few weak peaks centered at ca. 940, 1050 cm^{-1},[s2] probably due to the less PPy drafted on the graphene sheets.

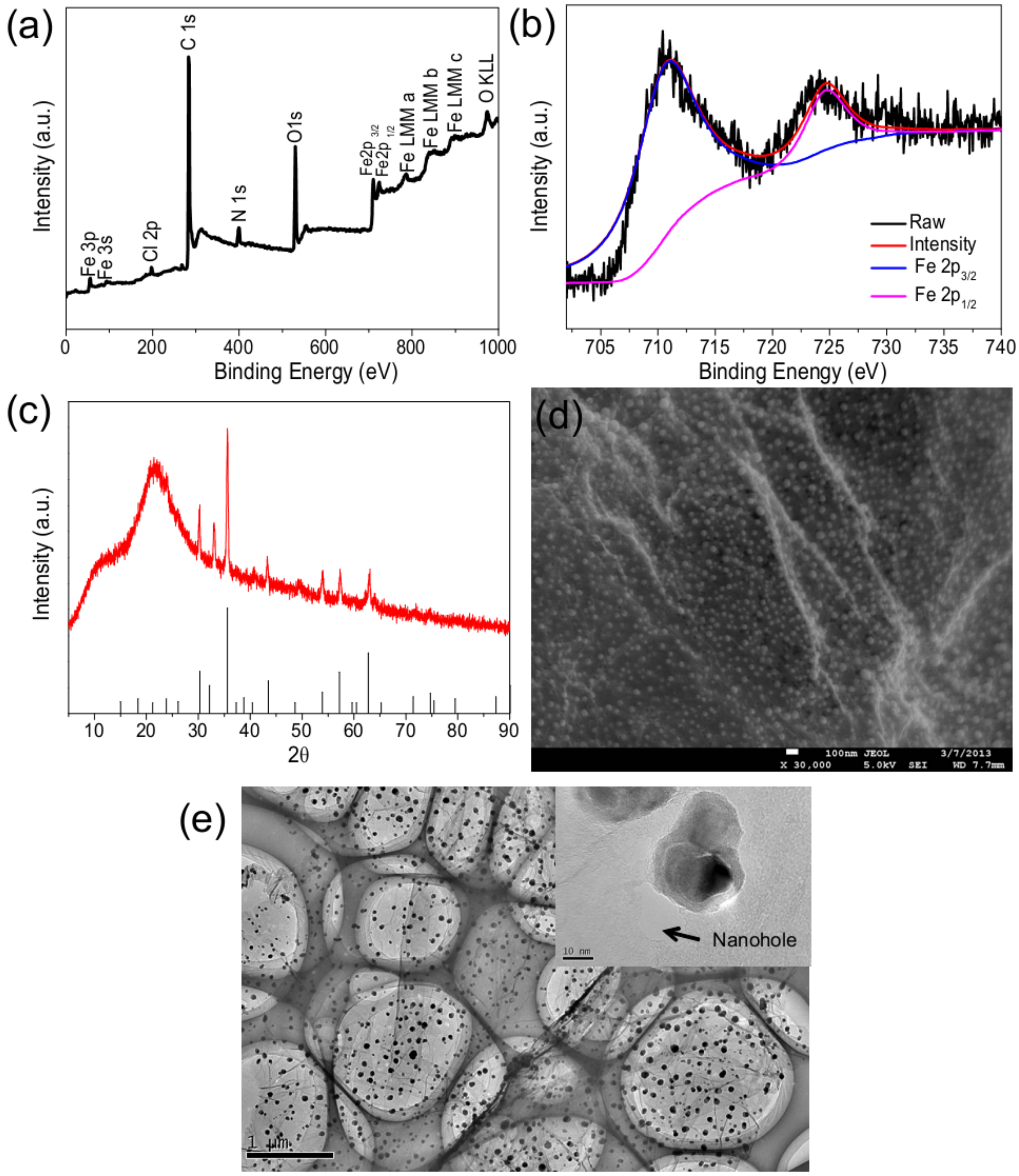

Figure S2. (a) XPS spectrum of N- doped graphene mesh@Fe_2O_3 foam after heating treatment. (b) The corresponding high-resolution Fe2p peak of (a). (c) XRD patterns of N-doped graphene mesh@Fe_2O_3 foam and the corresponding standard XRD pattern of Fe_2O_3 (below) (JCPDS ICCD card NO. 04-0755). (d, e) SEM and TEM images of the N-doped graphene mesh@Fe_2O_3 foam after heating treatment, inset of (e) is the corresponding magnified TEM image. Scale bar: d, 100nm; e, 1μm; inset of e, 10nm.

After heat treatment, $FeCl_3$ on the graphene sheets was decomposed into Fe_2O_3 to form N-GMF@Fe_2O_3 foam, which is confirmed by the XPS spectra and XRD (Figure S2a-c). The high-resolution Fe2p spectrum revealed two typical peaks of Fe2$p_{3/2}$ and Fe2$p_{1/2}$ belonging to the Fe_2O_3, which is according to the results of the XRD pattern (Figure S2b, c). SEM image showed that the Fe_2O_3 nanoparticals were uniform dispersed on the graphene sheets of the prepared N-GMF@Fe_2O_3 foam (Figure S2d), and visible nanoholes around the Fe_2O_3 nanoparticals were also confirmed by TEM (Figure S2e).

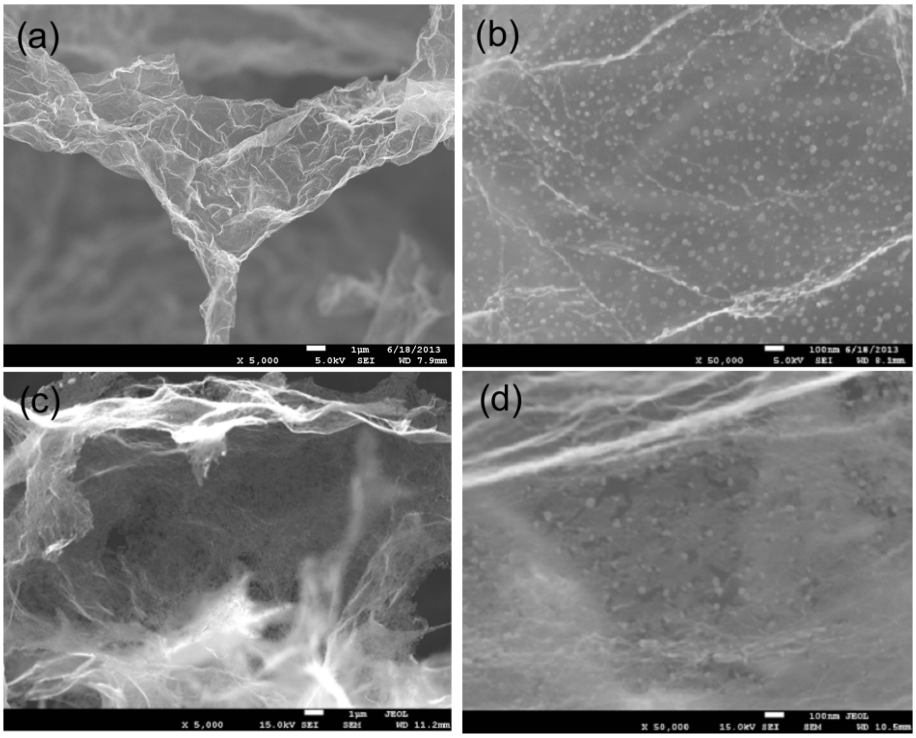

Figure S3. SEM images of the PPy/graphene@$FeCl_3$ foam under heat treatment at 500^{o}C for 1h (a) and (b). (c) and (d) are SEM images with heat treatment at 850^{o}C for 5h. Scale bar: a, c, 1μm; b, d, 100nm.

As shown in Figure S3a and b, during the heat treatment at temperature of below 500 ^{o}C, no any holes was observed around the Fe_2O_3 nanoparticles, indicating that Fe_2O_3 nanoparticles cannot react with its contacted graphene. When increasing the temperature to 850 ^{o}C, there were visible nanoholes appearing around the Fe_2O_3 nanoparticals on the graphene plane (Figure S2d). If increasing the time of heat treatment at 850 ^{o}C to 5h, there were a lot of large pores along the Fe_2O_3-graphene interfaces with no regular shape (Figure S3c and d).

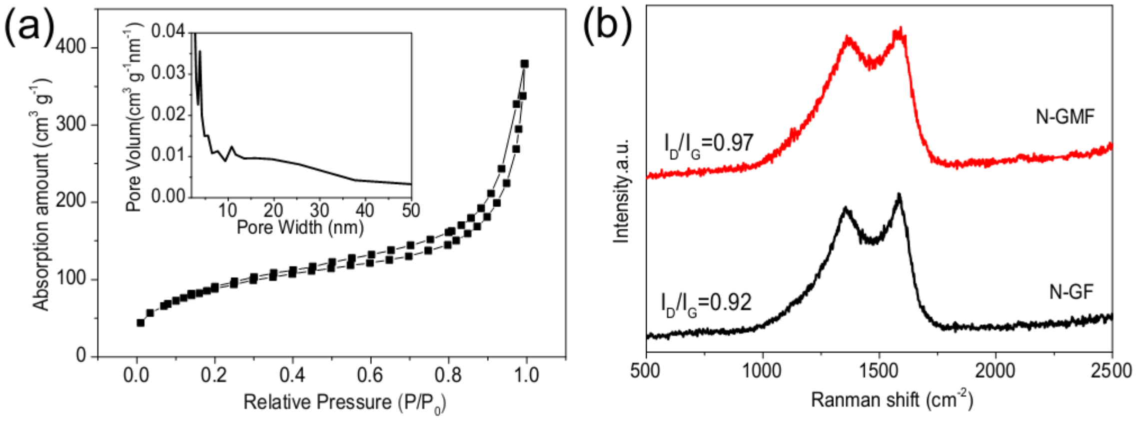

Figure S4. (a) The nitrogen adsorption-desorption isotherms of the N-GMF. Inset is the corresponding pore size distribution obtained by using Barrett–Joyner–Halenda (BJH) method. (b) Raman spectra of the N-GMF and N-GF, respectively.

The nitrogen-adsorption isotherm was shown in Figure S4a. The pore size distribution of the N-GMF was ranging from 0 to 40 nm (Inset of the Figure S4a), confirming the existence of mesopreos of N-GMF. Raman spectra of N-GMF (Figure S4b) shows two typical peaks, D band and G band centered at 1350 cm^{-1}and 1580 cm^{-1}, respectively. The I_D/I_G ratio of the N-

GMF was similar with that of the N-GF, showing that the appearance of the periodic nanoholes on the graphene basal plane did not cause an obvious effect on the crystalline structure of graphene. In Raman spectrum, Id/Ig ratio of N-GMF is believed to be related to the density of defects in the nanomesh and its edge roughness.[s3] Here, The Id/Ig ratio of N-GMF is just slightly higher than mesh-free graphene foam, which probably is because the introduction of nanoholes with smoothing edges on the graphene sheets did not damage the intrinsic crystalline structure of graphenes (Figure S5).

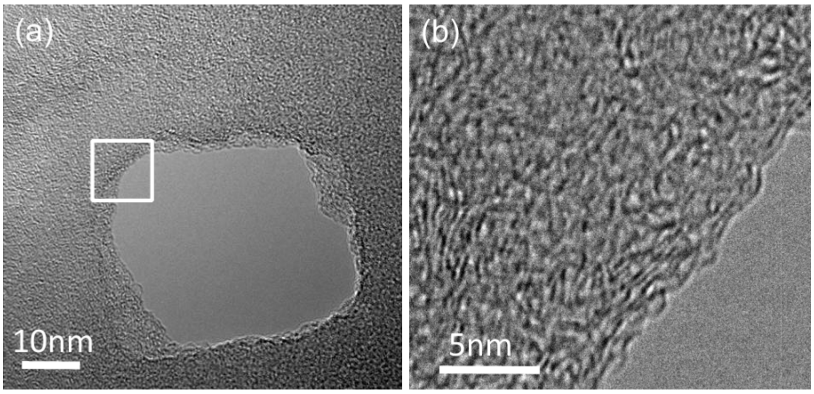

Figure S5. (a) The High resolution TEM images of N-GMF with single nanopore. (b) The corresponding enlarged image of the area that noted with white square of (a).

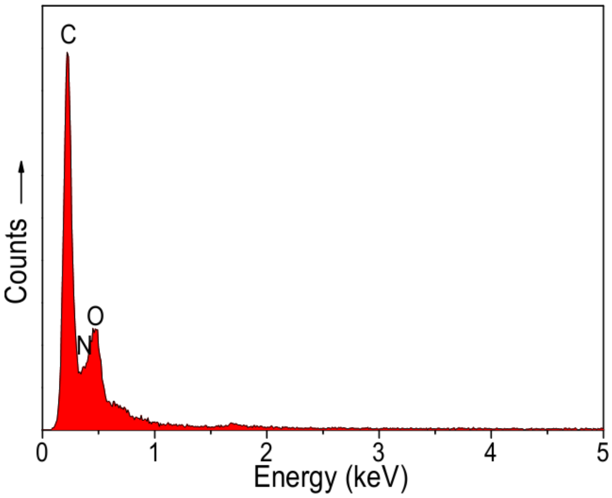

Figure S6. EDS spectrum of N-GMF.

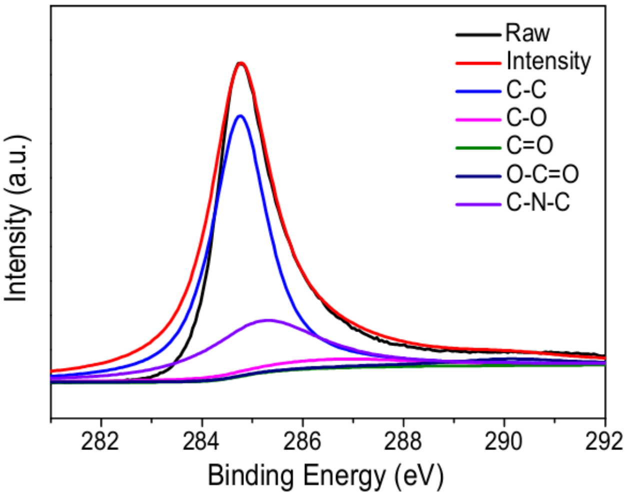

Figure S7. High-resolution XPS spectra of C 1s for the N-GMF.

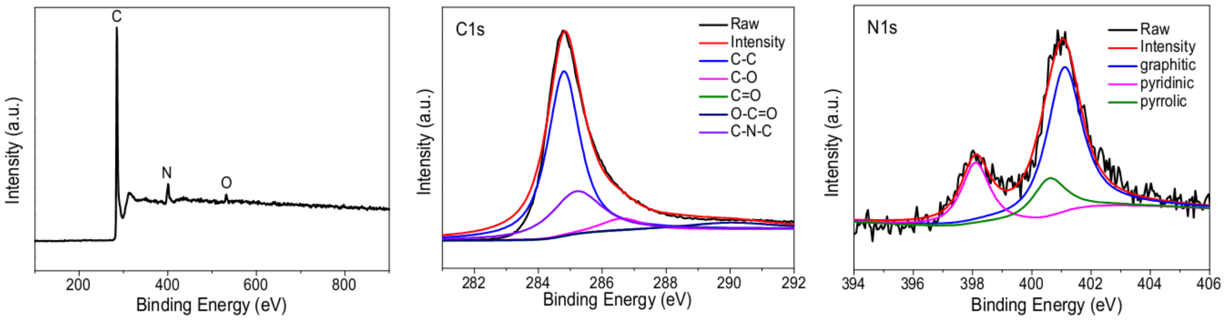

Figure S8. XPS spectrum and high-resolution C 1s and N 1s peaks of the N-GF.

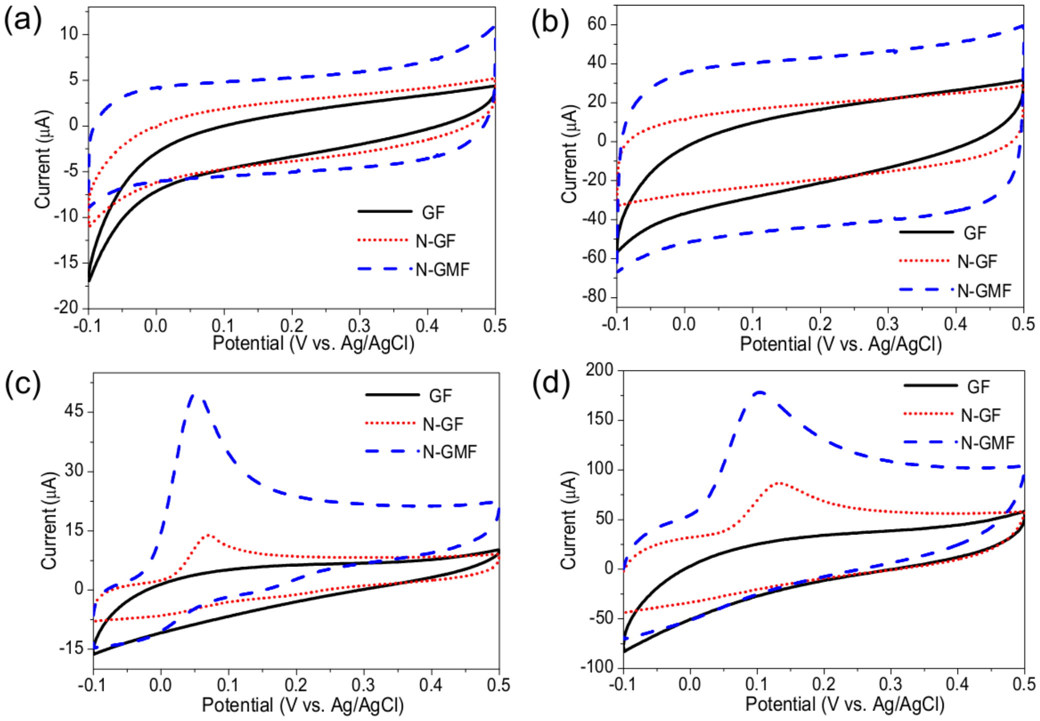

Figure S9. (a) and (b) CV curves of GF, N-GF and N-GMF with the mass loading of ~16μg in the electrolyte of 0.1 M phosphate buffered saline (PBS) solution containing 0.1 M KCl with the scan rate of 10 mV s^{-1} and 100 mV s^{-1}, respectively. (c) and (d) CVs corresponding to those in (a) and (b) with additional 5 mM AA.

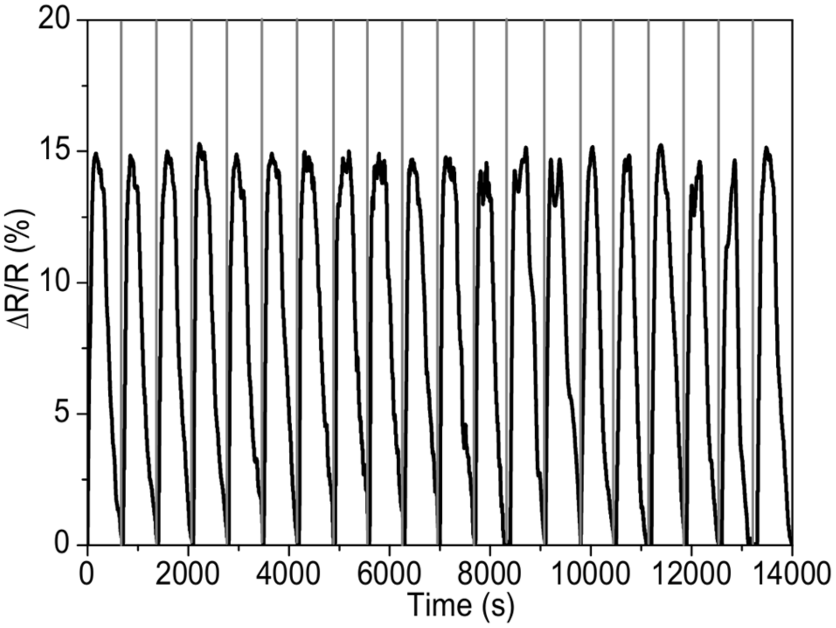

Figure S10. The cycling response of N-GMF to 400 ppm of NH_3. ΔR and R stand for the resistance change and the initial resistance.

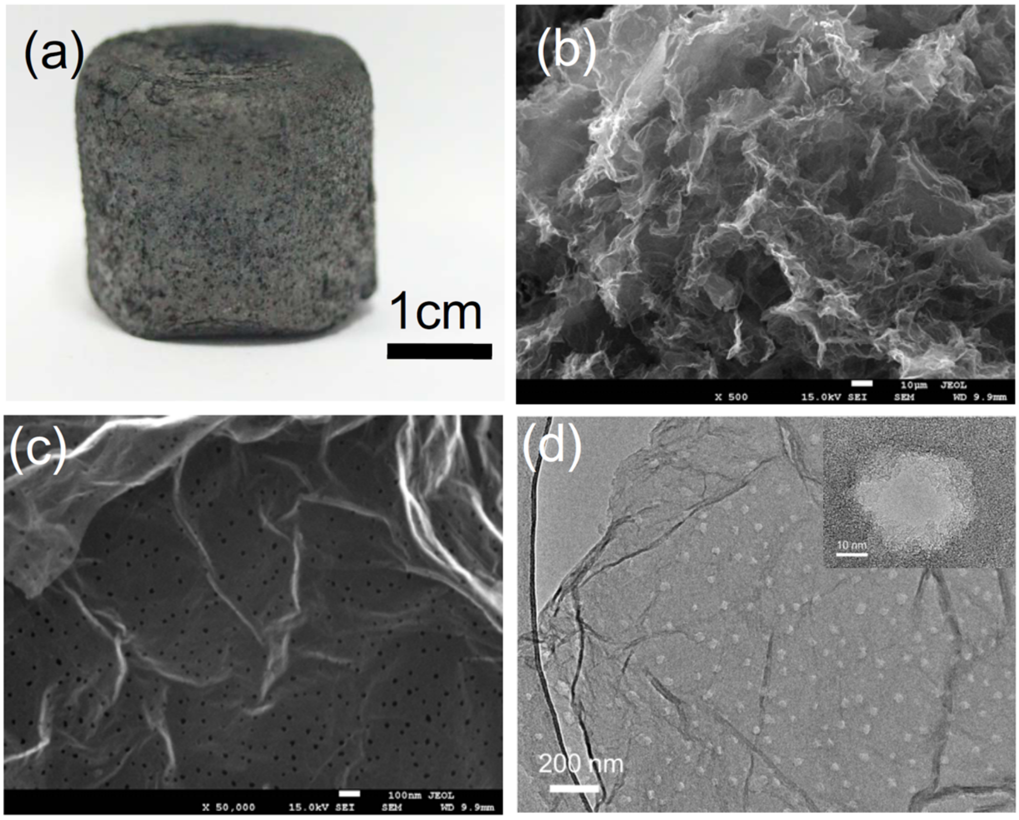

Figure S11. (a) Photograph of as-prepared N-S-GMF. (b) SEM image of the N-S-GMF. (c) The amplified view of the (b). (d) TEM image of the sheets within the N-S-GMF. Inset is the enlarged image of single nanohole.

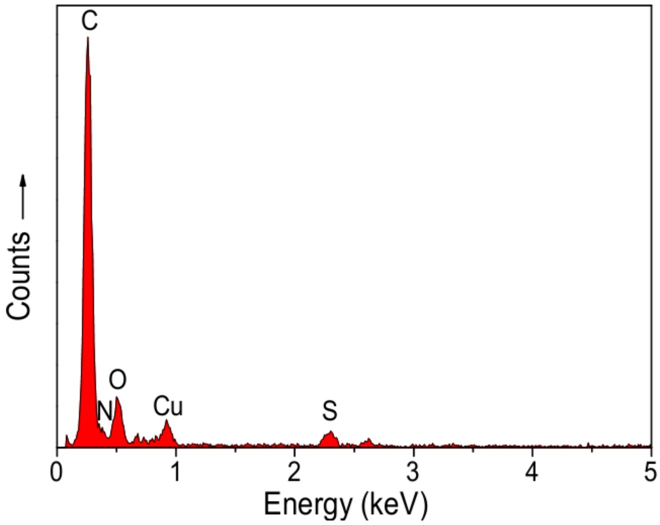

Figure S12. EDS spectrum of the N-S-GMF.

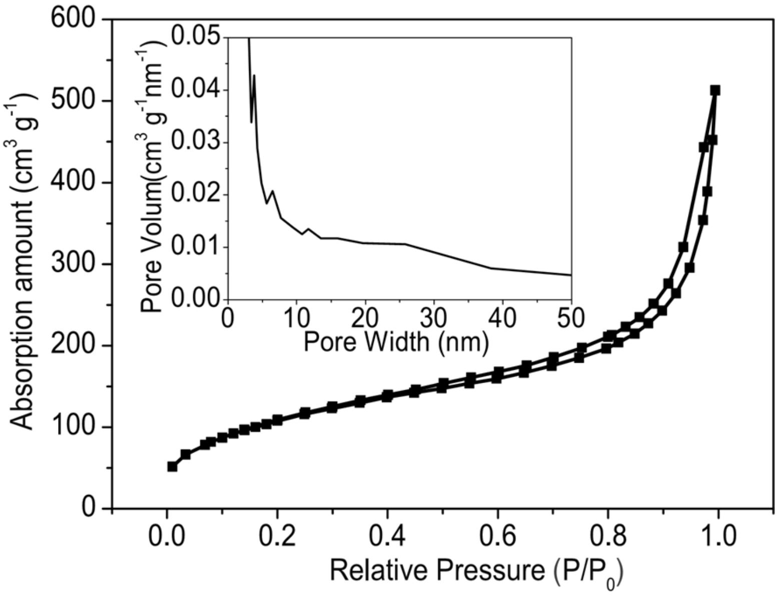

Figure S13. The nitrogen adsorption-desorption isotherms of the N-S-GMF. Inset is the corresponding pore size distribution obtained by using BJH method.

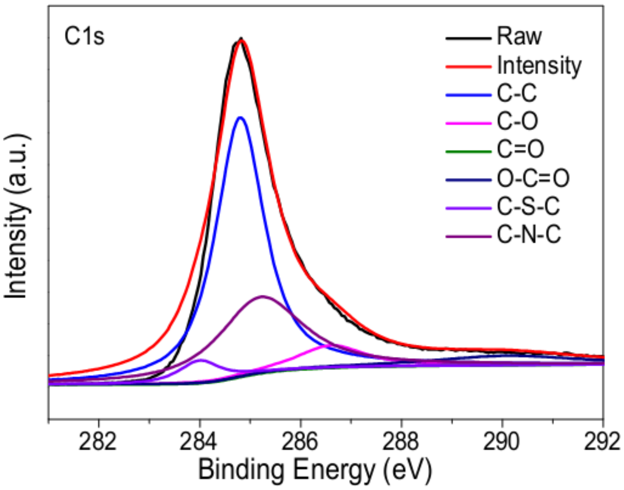

Figure S14. High-resolution XPS spectra of C 1s for the N-S-GMF.

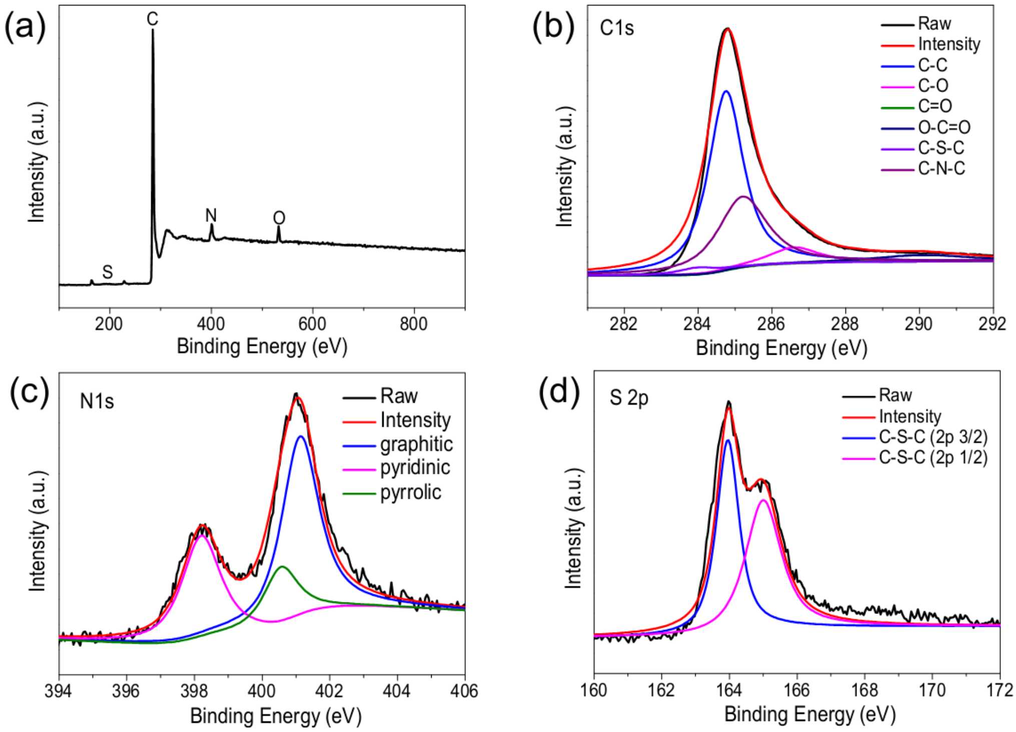

Figure S15. XPS spectrum (a) and high-resolution C1s (b), N 1s (c) and S 2p (d) of the N-S-GF.

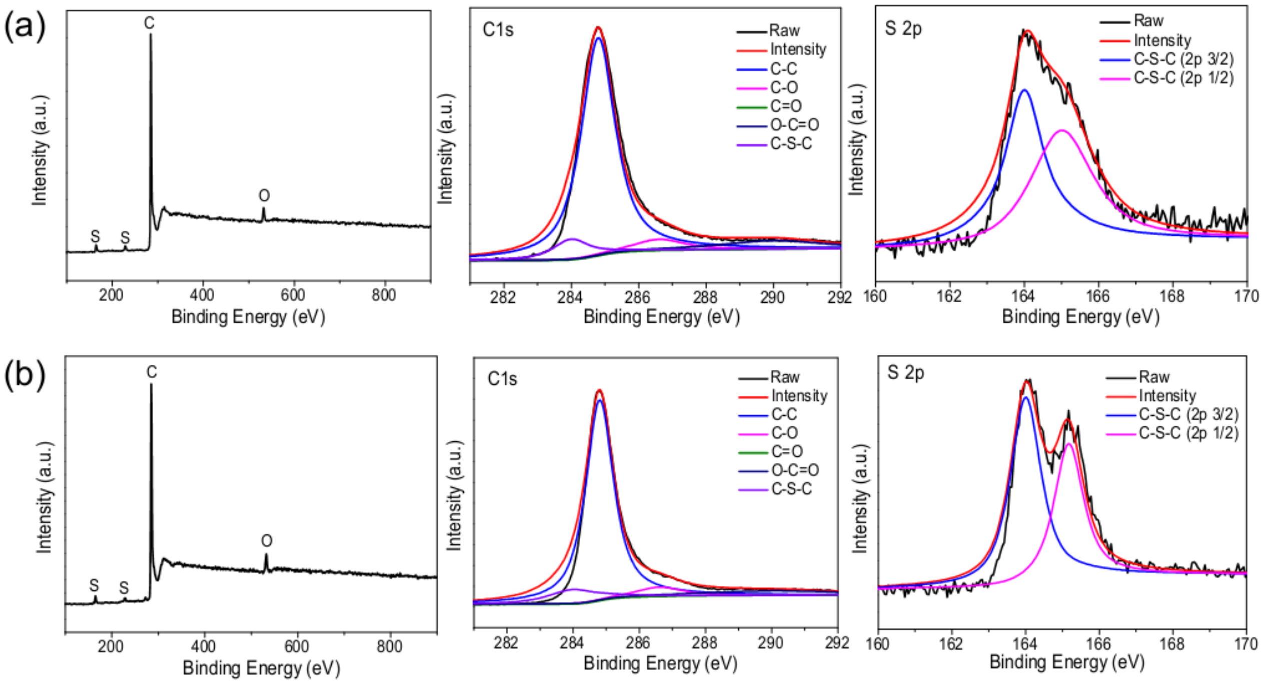

Figure S16. Survey and high-resolution XPS spectra of (a) the S-GMF and (b) the S-GF.

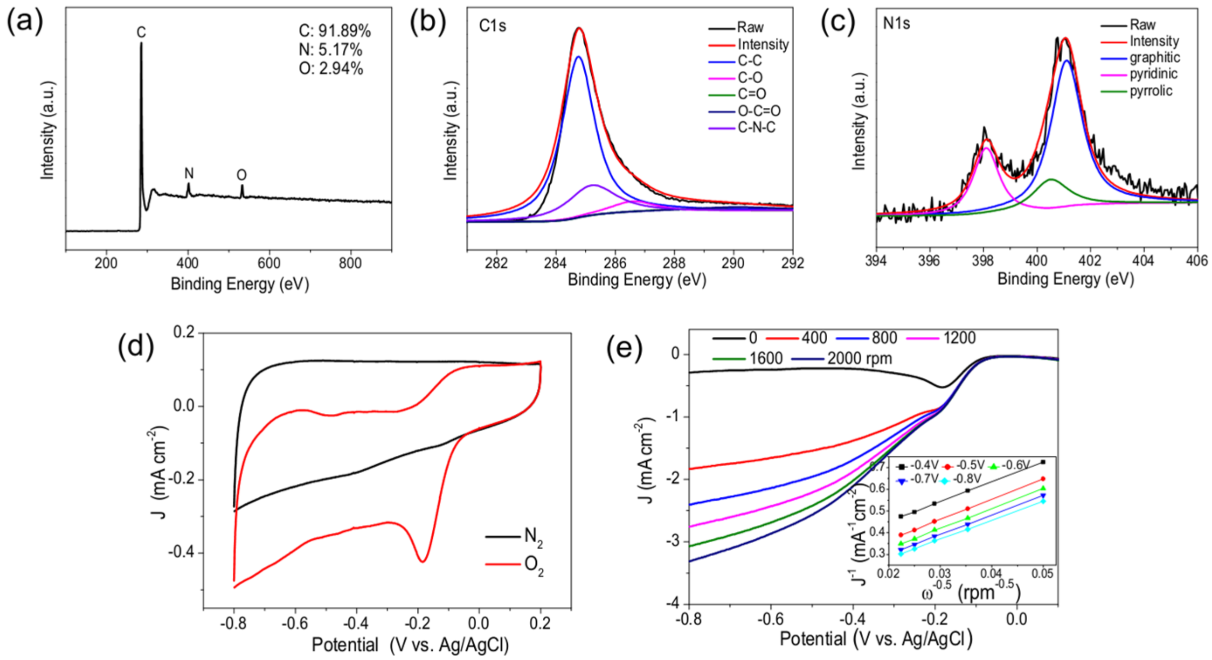

Figure S17. (a) XPS spectrum of N-GMF with the N content of ~5.2%. (b) and (c) the corresponding high-resolution C1s and N1s peak, respectively. (d) CV curves of N-GMF in a N_2 and O_2-saturated 0.1 M KOH solution at scan rate of 10 mV/s, respectively. (e) LSV curves of N-GMF in O_2-saturated 0.1 M KOH solution at different rotating speeds from 0 rpm to 2000 rpm. Inset of (e) the corresponding Koutecky-Levich plots derived from LSV curves at different potentials from -0.4V to -0.8V.

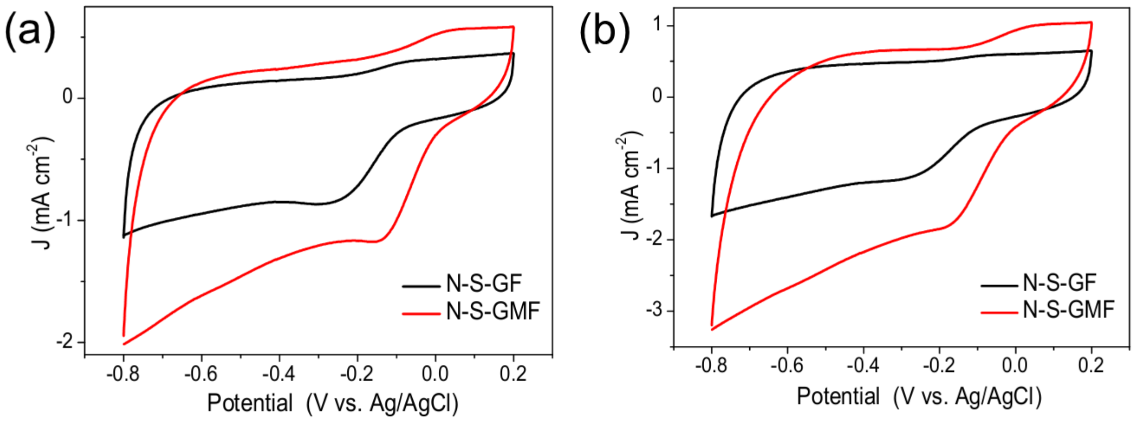

Figure S18. CV curves of the N-S-GF and N-S-GMF in O_2-saturated 0.1M KOH at the scan rate of 50mV/s (a) and 100mV/s (b), respectively.

Cycle voltammograms (CVs) for the N-S-GF and N-S-GMF were also investigated (Figure S18). As shown in Figure S18a, the N-S-GMF shows an obvious redox peak centered at ca. -

0.14V which is more positive than that of the N-S-GF (centered at ca. -0.24V). Even at high scan rate of 100mV/s, the N-S-GMF exhibits excellent reduction peak at ca. -0.18V better than that of the N-S-GF (ca. -0.27V) (Figure S18b).

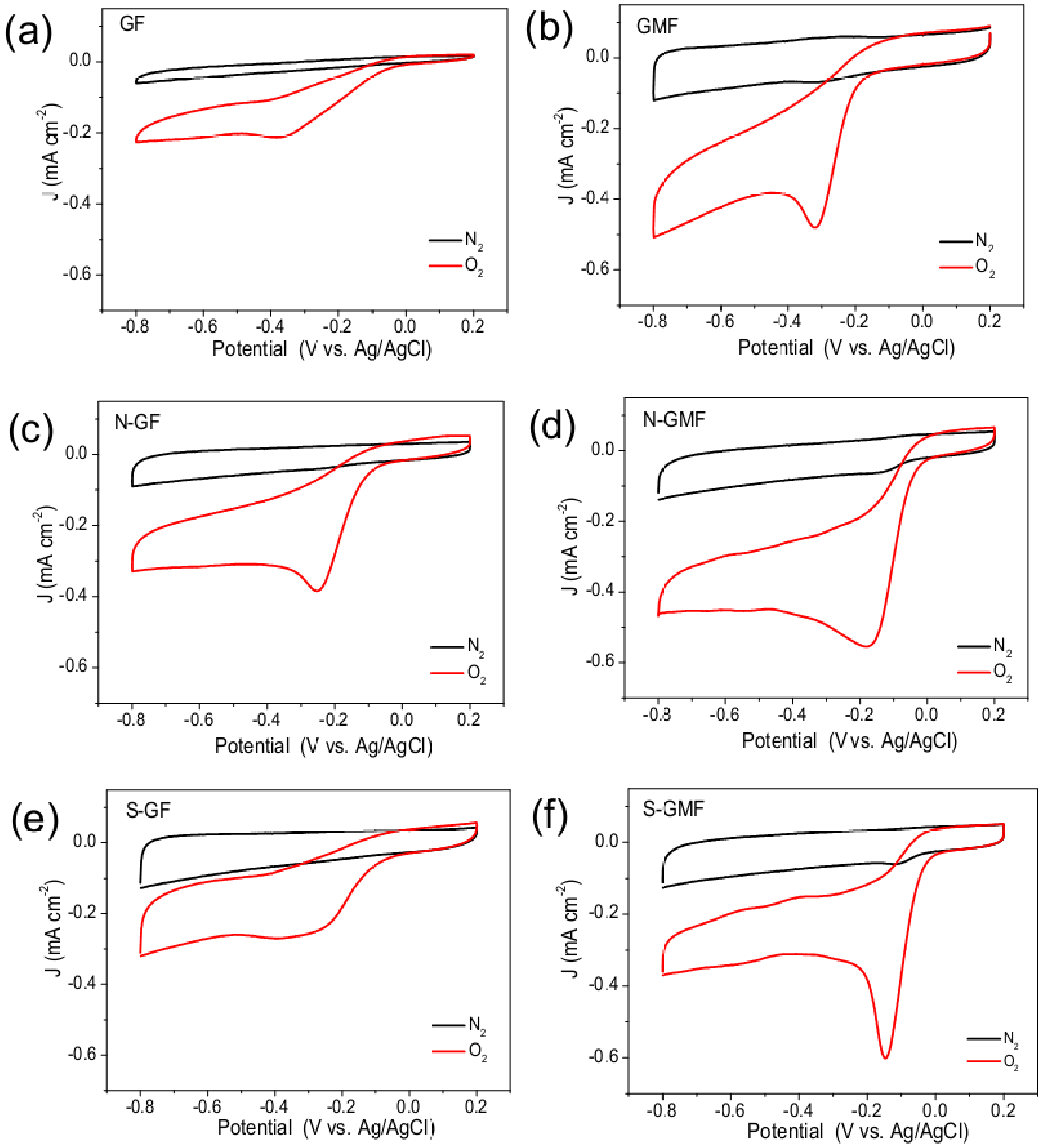

Figure S19. CV curves of the GF (a), GMF (b), N-GF (c), N-GMF (d), S-GF (e) and S-GMF (f) in N_2- or O_2-saturated 0.1 M KOH solution. The scan rate is 10 mV/s.

The CV curves of comparable catalysts for the GF, S-GF, N-GF, N-S-GF, GMF, N-GMF and S-GMF were shown in Figure S19. The graphene mesh foams show a higher oxygen reduction current and more positive ORR peaks than those mesh-absent normal doped graphene materials

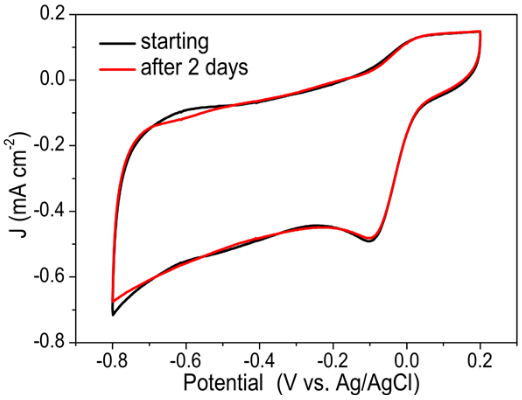

Figure S20. Electrochemical durability of N-S-GMF with continuous cyclic voltammetry in O_2-saturated 0.1 M KOH. Scan rate is 10mV/s.

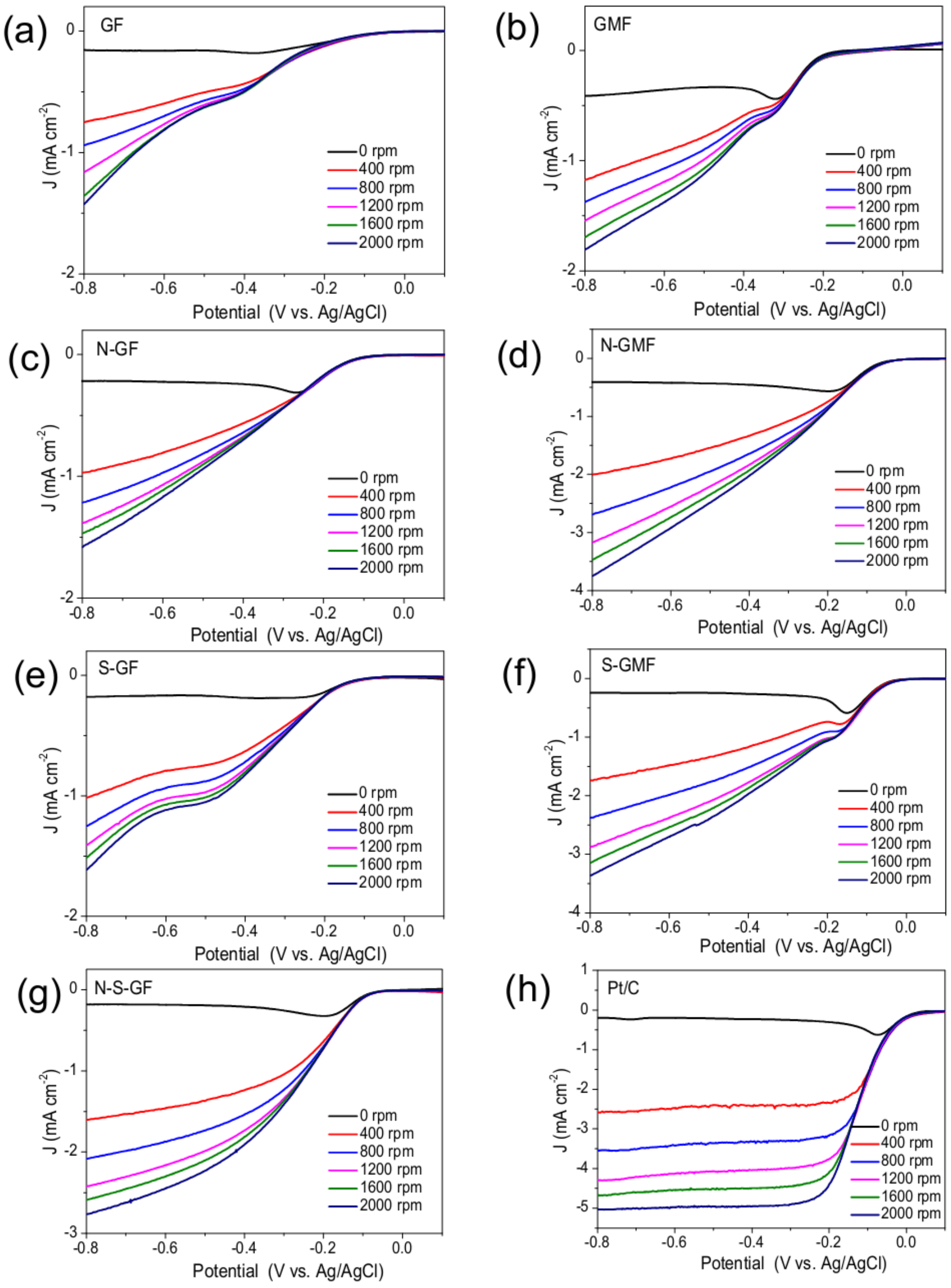

Figure S21. LSV curves of the GF (a), GMF (b), N-GF (c), N-GMF (d), S-GF (e), S-GMF (f), N-S-GF (g) and Pt/C (h) in O_2-saturated 0.1 M KOH solution at different rotating speeds from 0 rpm to 2000 rpm. The scan rate is10 mV/s.

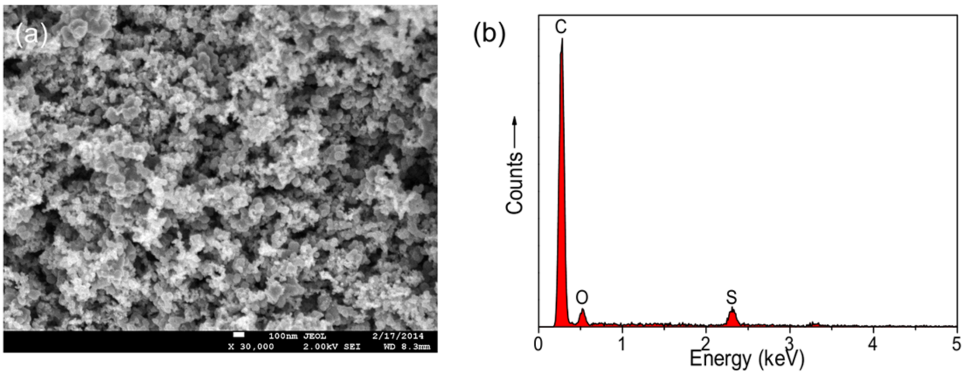

Figure S22. (a) The SEM images of S-Vulcan Carbon. (b) The corresponding EDS spectrum of (a).

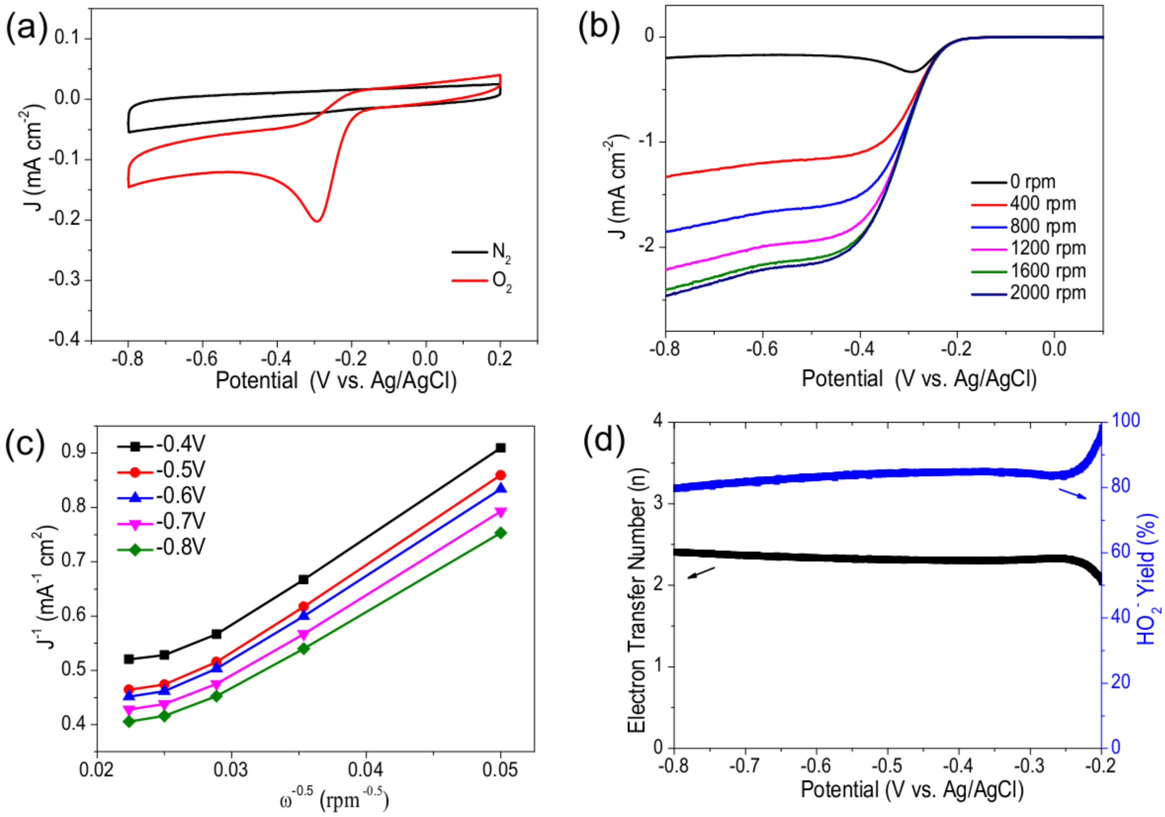

Figure S23. (a) CV curve of the S-doped Vulcan carbon in N_2- or O_2-saturated 0.1 M KOH solution. The scan rate is 10 mV/s. (b) LSV curves of the S-doped Vulcan carbon in O_2-saturated 0.1 M KOH solution at different rotating speeds. The scan rate is 10mV/s. (c) The

Koutecky-Levich plots derived from LSV curves at different potentials from -0.4V to -0.8V. (d) HO_2^- production and the corresponding *n* of the S-doped Vulcan carbon.

As shown in Figure S23a, the S-doped Vulcan carbon shows a more negative O_2 reduction peak at ca. -0.28V than doped GMFs in an O_2-saturated 0.1 M KOH solution (Figure 5a and Figure S19). The linear sweep voltammograms (LSVs) shown in Figure S23b measured on a rotating disk electrode (RDE) for S-Vulcan Carbon have much more negative potentials and lower ORR reaction current than of doped GMFs (Figure S21). The mean transferred electron number (*n*) per oxygen molecule calculated from the slope of the Koutecky–Levich (K-L) plots (Figure S23b and c) is about 2.0 indicating the two-electron pathway for the ORR. The rotating ring–disk electrode (RRDE) measurement was also performed shown in Figure S23d. The S-doped Vulcan carbon shows a high peroxide yield of 80% at all potential range further confirmed the 2e ORR process.

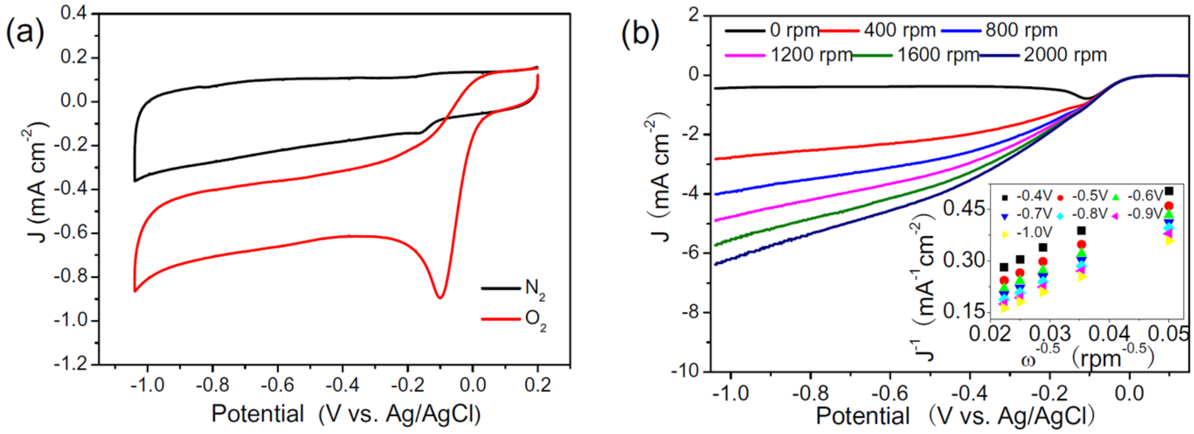

Figure S24. (a) CV curves of N-S-GMF (with the mass loading of 0.16 mg/cm^2) in an N_2- and O_2-saturated 0.1 M KOH solution at scan rate of 10 mV/s, respectively. (b) LSV curves of the N-S-GMF in O_2-saturated 0.1 M KOH solution at different rotating speeds. The scan rate is 10mV/s. Inset shows the Koutecky-Levich plots derived from LSV curves at different potentials from -0.4V to 1.0 V.

As shown in Figure S24a, The N-S-GMF catalyst with the mass loading of 0.16 mg/cm^2 exhibits still excellent O_2 reduction peak at ca. -0.09V in an O_2-saturated 0.1 M KOH solution, similar with the N-S-GMF (with the mass loading of 0.08 mg/cm^2). The LSV curves of N-S-GMF shown in Figure S24b indicate that the diffusion current densities increased with increasing the rotation speed. The diffusion limiting current can be obtained when expending the potential to around 1.0 V. The mean transferred electron number (*n*) per oxygen molecule calculated from the slope of the Koutecky–Levich (K-L) plots (Figure S24b, inset) using the K–L equation [Eq. (S1 and S2)] is approximately 3.7, indicating a nearly four-electron pathway for the ORR.

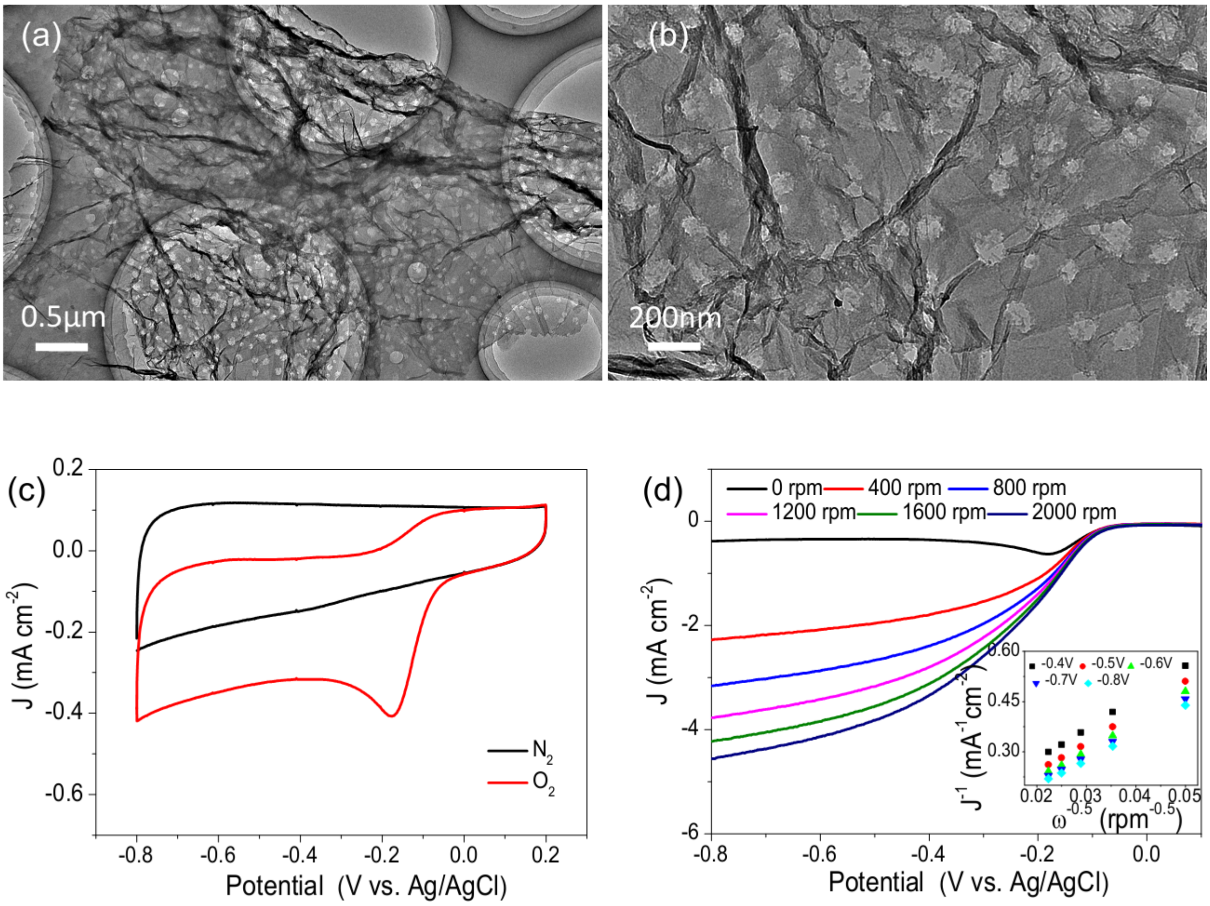

Figure S25. (a) and (b) The TEM images of N-S-GMF with the size of the nanomesh more than 100nm. (c) The CV curves of N-S-GMF with the size of the nanomesh more than 100nm in N_2- or O_2-saturated 0.1 M KOH solution at scan rate of 10 mV/s. (d) The LSV curves in O_2-saturated 0.1 M KOH solution at different rotating speeds from 0 rpm to 2000 rpm. The scan rate is10 mV/s. Inset is the Koutecky-Levich plots derived from LSV curves at different potentials from -0.4V to -0.8V. Scale bars: a, 0.5 μm; b, 200 nm).

We adjust the size of the pore in mesh materials by slightly increasing the heat-treating time at 3h. As shown in Figure S25a&b, the pore size of the N-S-GMF is more than around 100nm when the treating time expended at 3h. The ORR activity of the GMF decreases when the size of the mesh increases out of 100nm. The N-S-GMF with a relatively larger pore size shows a much more negative O_2 reduction peak at ca. -0.17 V than that with a smaller pore size (ca. -0.1V) in an O_2-saturated 0.1 M KOH solution shown in Figure S25c and Figure 5a. The onset potential of N-S-GMF with the mesh-size more than 100nm obtained from LSV curves falls to -0.03V (Figure S25d) and the calculated *n* turns out to be 3.3 indicating the two and four electron way for N-S-GMF (with the mesh-size more than 100nm). This can be ascribed to that the decreasing of the density of the nanoholes for N-S-GMF with the size of the mesh more than100 nm (about 2.4×10^7 hole/cm^2) may lead to the reduction of the active edges contacting with the electrolyte.

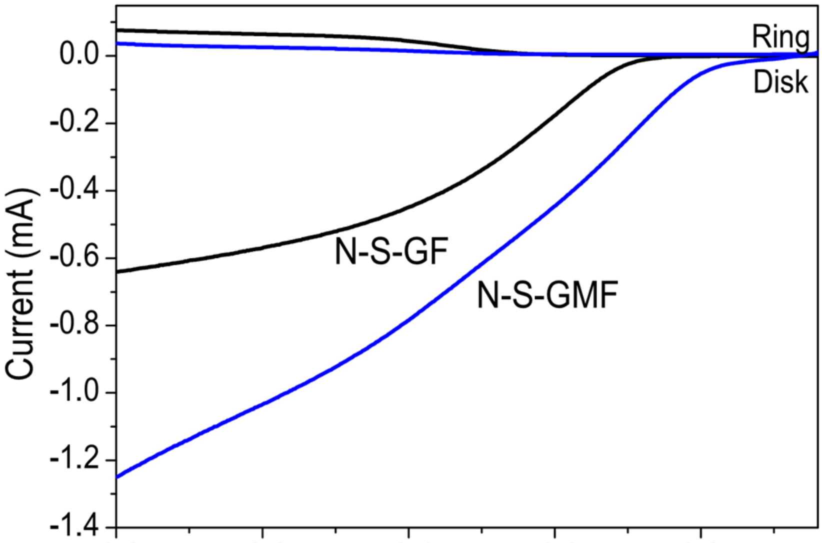

Figure S26. RRDE curves of the N-S-GF and N-S-GMF at 1600 rpm.

We performed rotating ring-disk electrode (RRDE) voltammograms to investigate the electrochemical procedures of the ORR on N-S-GF and N-S-GMF in the 0.1M KOH (Figure S26). The current responses for the oxidation of hydrogen peroxide ions (HO_2^-) measured with a Pt ring electrode at the potential of 0.50 V are also included in Figure S26. The N-S-

GMF exhibits higher current and more positive reduction peak than the N-S-GF. Besides, the N-S-GMF shows a one-step process suggesting a four-electron pathway for the ORR consistent with the calculated electron transfer numbers (n).

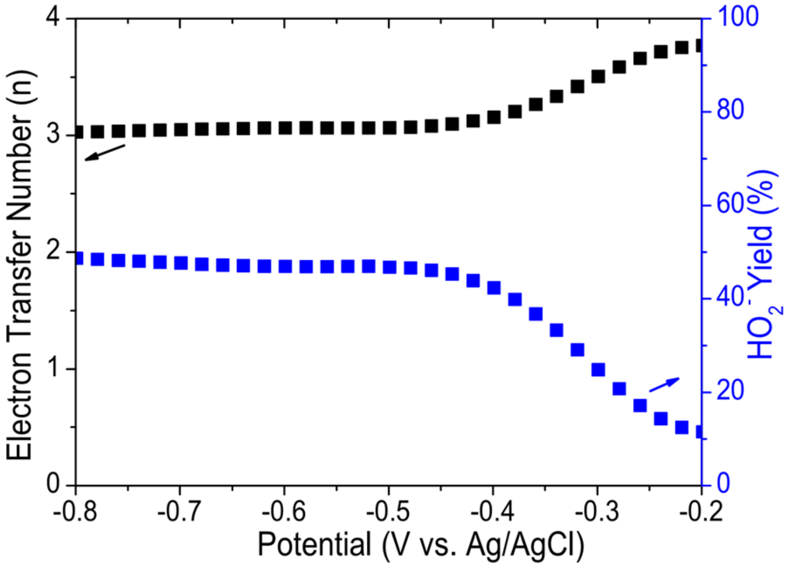

Figure S27. HO_2^-production and the corresponding electron-transfer number of the N-S-GF.

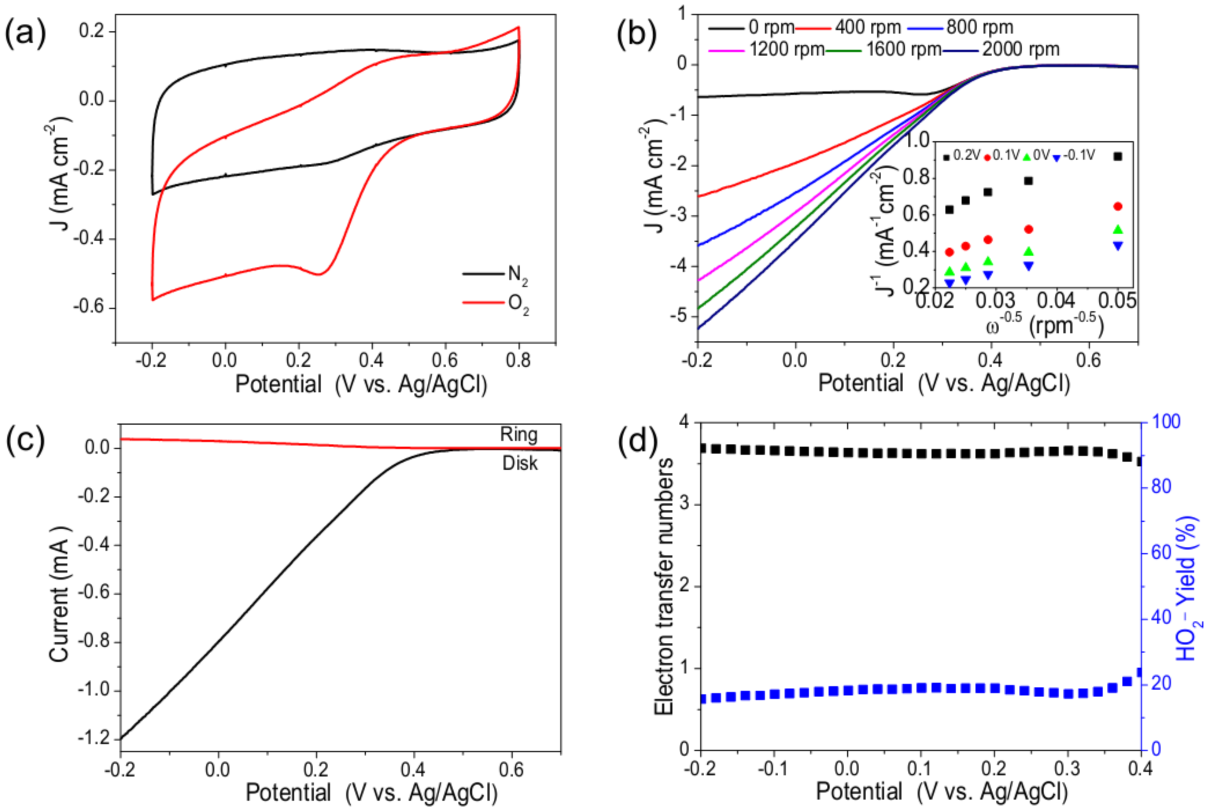

Figure S28. The ORR performance for N-S-GMF in acidic solution. (a) CV curves of N-S-GMF in an N_2- and O_2-saturated 0.5 M H_2SO_4 solution at scan rate of 10 mV/s, respectively. (b) LSV curves of the N-S-GMF in O_2-saturated 0.5 M H_2SO_4 solution at different rotating speeds. The scan rate is 10mV/s. Inset shows the Koutecky-Levich plots derived from LSV curves at different potentials from 0.2V to -0.1V. (c) RRDE curves of the N-S-GMF at 1600 rpm. (d) HO_2^- production and the corresponding *n* of the N-S-GMF.

The ORR performance of the N-S-GMF material (with the mass loading of 0.08mg/cm^2) was also investigated in acidic solution as shown in Figure S28. In Figure S28a, the N-S-GMF shows a significant reduction peak at about 0.27 V in the presence of oxygen, while no obvious response was observed at the same potential range under N_2. The LSVs curves of the N-S-GMF at different electrode rotation rates were also investigated on the RDE in an O_2-saturated 0.5 M H_2SO_4 solution (Figure S28b). The mean *n* value for the N-S-GMF is calculated to be 3.45 (Figure S28b inset), suggesting a nearly four-electron process for the ORR on the N-S-GMF electrode.

The RRDE voltammogram was also investigated in the 0.5M H_2SO_4 (Figure S28c). The oxidation of hydrogen peroxide ions (HO_2^-) measured with a Pt ring electrode at the potential of 1.0 V was also shown in Figure S28d. The N-S-GMF shows a one-step process suggesting a four-electron pathway for the ORR consistent with the calculated electron transfer numbers (n).

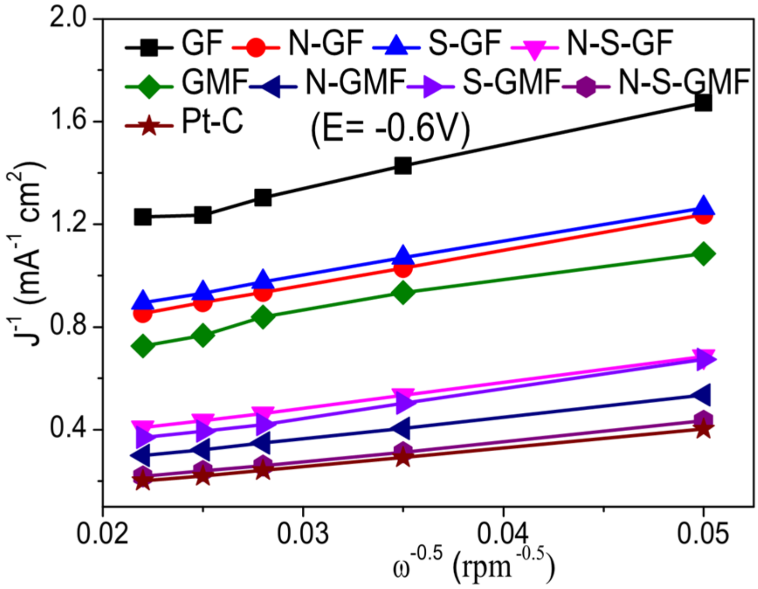

Figure S29. The K-L plots derived from LSV curves at the potential of -0.6V.

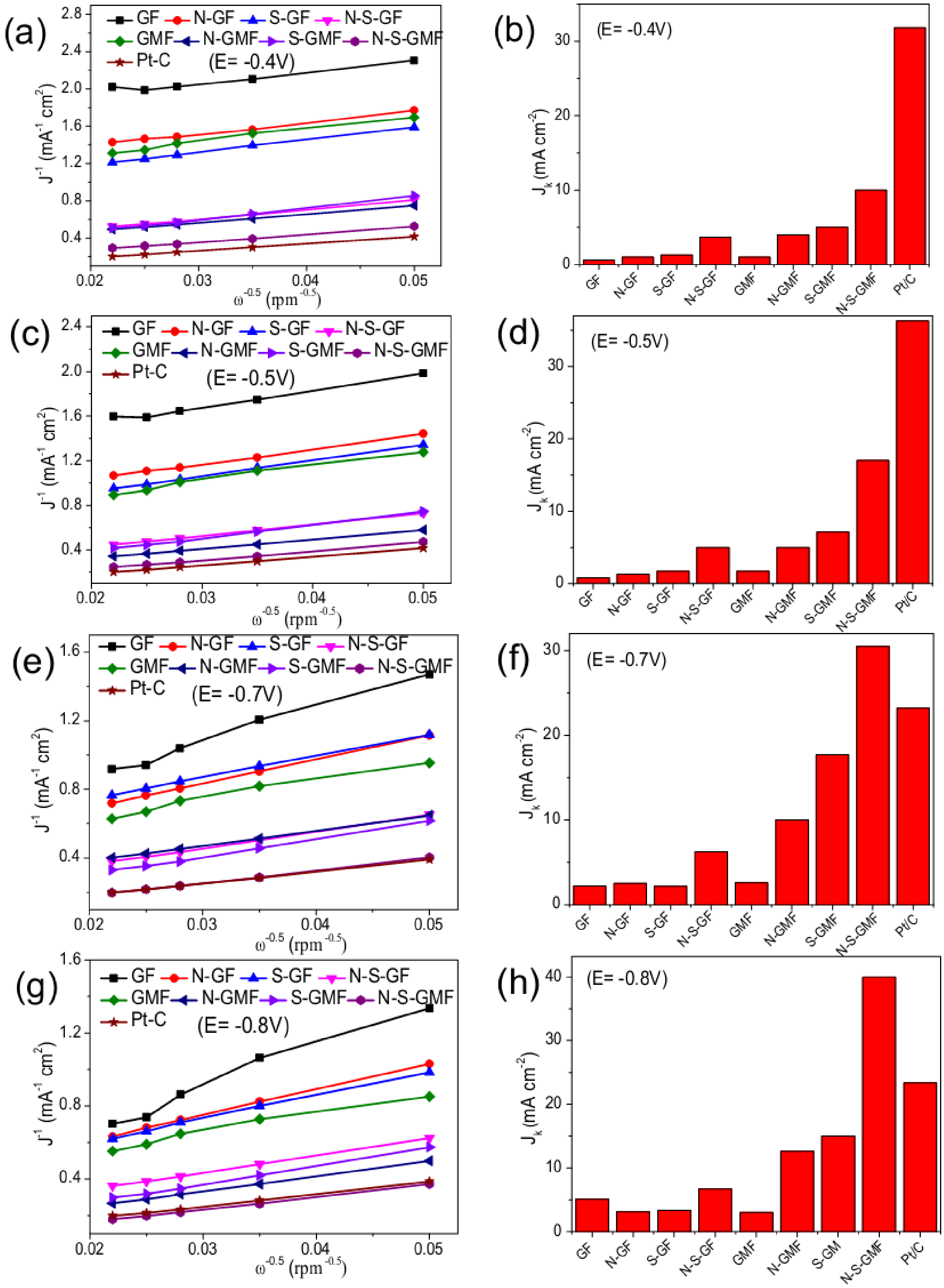

Figure S30. K-L plots and the corresponding kinetic limiting currents at the different potential of -0.4 V (a) and (b), -0.5 V (c) and (d), -0.7 V (e) and (f), -0.8 V (g) and (h), respectively.

The Koutecky–Levich (K-L) plots were derived from LSV curves at -0.4, -0.5, -0.7 and -0.8 V at various rotating speeds shown (Figure S30 a, c, e and f). The graphene mesh assembles showed good linearity. Specially, the prepared N-S-GMF showed a much high ORR current close to the commercial Pt/C electrode and obvious larger than all the other compared catalysts. The corresponding kinetic limiting currents (J_k) values were also obtained from the intercept of K-L plots (Figure s30b, d, f, h). Notably, the J_k of the N-S-GMF was superior to that of N-S-GF and other comparable catalysts over the whole potential range (from -0.4 to -0.8V), and even exceeded the Pt/C catalyst at high potential range (from -0.7 to -0.8V), indicating the high ORR performance for the N-S-GMF materials.

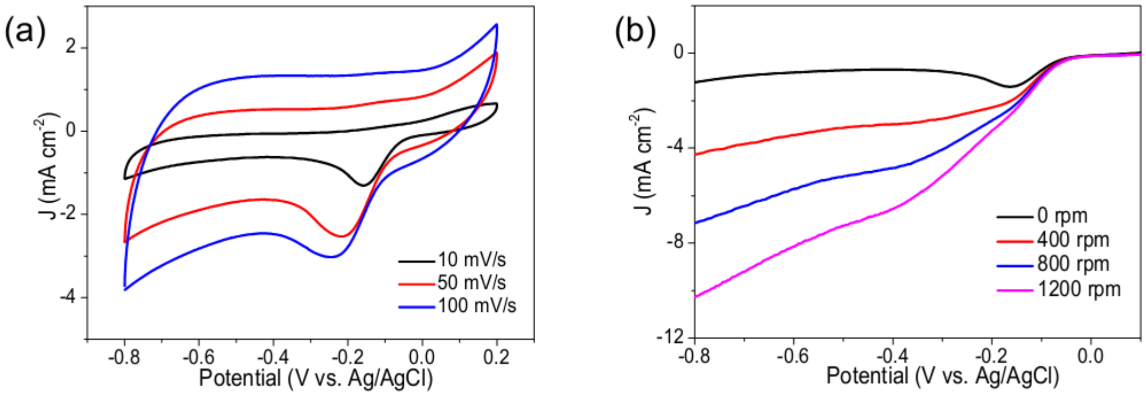

Figure S31. (a) The CV curves of N-S-GMF (mass loading is about 0.35 mg/cm^2) in O_2-saturated 0.1 M KOH solution from the scan rate of 10 to 100 mV/s. (b) The LSV curves in O_2-saturated 0.1 M KOH solution at different rotating speeds from 0 rpm to 1200 rpm. The scan rate is10 mV/s.

The ORR properties for the graphene mesh materials (N-S-GMF as example) which was directly adhered to the glass carbon electrode instead of dispersing the N-S-GMF into ethanol was also investigated. The N-S-GMF was cut into a wafer with the area of 0.25cm^2 and the thickness of 0.7mm, and fixed on the glass carbon electrode (with the area of 0.25cm^2) using 10μl Nafion solution (5%) and dried in air. As shown in Figure S31a, the N-S-GMF shows a obvious reduction peak from the scan rate of 10 to 100 mV/s.

The peak of N-S-GMF centered at ca. -0.155V at 10mV/s is slightly negative than N-S-GMF (ca. -0.1V) diepersed in the ethanol, probably due to the bulk materials for N-S-GMF didn't fully contact with oxygen dissolved in the electrolyte and the properties of the bulk materials can't be well represented. The LSV curves were shown in Figure S31b, the diffusion current densities increased with increasing the rotation speed. However, the part of bulk materials dropped out when the rotation speed was up to 1600 rpm. Thence, only the LSV data of N-S-GMF below the 1200 rpm was obtained.

Table S1. Brunauer–Emmett–Teller (BET) surface areas, Barrett–Joyner–Halenda (BJH) pore volumes of catalysts.

Samples	**BET surface Area (m^2 g^{-1})**	**BJH adsorption pore volume (mL g^{-1})**	**Porosity(%)**
N-S-GMF	405	0.60	~99.77
N-GMF	362	0.44	~99.79
S-GMF	280	0.41	~99.64
GMF	310	0.50	~99.60
N-S-GF	207	0.35	~99.20
N-GF	186	0.39	~99.40
S-GF	164	0.20	~98.80
GF	151	0.24	~98.10

The porosities of graphene catalysts shown in Figure table S1 were calculated based on the equation:

$$\varepsilon=1-\rho/\rho_o$$

where ε represent the porosity, ρ is the density of the as prepared graphene materials while ρ_o is the density of graphite which is assumed to be 2.2 g cm^{-3}.[s4, s5]

Table S2. The elements content (atomic %) of different catalysts determined by XPS analysis.

Materials	C %	O%	N%	S%
N-S-GF	91.51	2.48	5.12	0.89
N-GF	91.48	1.96	6.56	
S-GF	94.28	4.2		1.52
N-GMF	91.29	1.93	6.78	
S-GMF	95.37	3.12		1.51
N-S-GMF	91.13	2.83	5.05	0.99

Table S3. ORR electrocatalytic performance of graphene-based materials and typical porous carbon-based materials in alkaline solution.

Materials	Loading (mg/cm^2)	Scan rate (mV/s)	Reductionpeak (vs Ag/AgCl)	Onset potential (vs Ag/AgCl)	Ref.
N-S-GMF	**0.08**	**10, 50, 100**	**-0.1V , -0.14V, -0.18V**	**0.04V**	**Present work**
N-S-doped Graphene	unknown	100	-0.24V	-0.06V	[s6]
N-B-doped Graphene	0.28	100	-0.25V	unknown	[s7]
N-doped Graphene	unknown	100	~-0.3V	-0.1	[s8]
S-doped Graphene	unknown	unknown	-0.29V	unknown	[s9]
S-Graphene Nanoplatelets	0.076	50	-0.4V	-0.22V	[s10]
N-doped Graphene Framwork	0.012	50	~-0.3V	-0.18V	[s11]
N-doped Graphene	~0.04	100	-0.32V	-0.04V	[s12]

N-S-doped Few Layer Graphene Oxide	0.306	50	-0.18V	-0.11V	[s13]
N-doped Ordered Macro-Mesoporous Carbon/Graphene	0.417	50	~0.28V	-0.05V	[s14]
N-doped Graphene	Unknown	50	-0.36V	unknown	[s15]
Macro-/Mesoporous Co-containing N doped carbon materials	Unknown	10	-0.24V	-0.09V	[s16]
Nitrogen-Doped Carbon Nanocages	0.08	10	-0.22V	-0.13V	[s17]
Sulfur and Nitrogen -doped, Ordered Mesoporous Carbons	0.306	50	-0.16V	-0.05V	[s18]
Sulfur–Nitrogen co-doped Carbon Foams	0.142	Unknown	-0.20V	Unknown	[s19]
Mesoporous Nitrogen-Doped Carbons	0.82	50	-0.19V	0.035V	[s20]
Porous Carbon Nanosheets (PCNSs)	0.11	50	-0.21V	-0.02V	[s21]
Nitrogen-doped Nrdered Macro-Mesoporous Carbon/ Graphene (N-OMMC-G) hybrid	0.42	50	Unknown	-0.05V	[s22]
Nitrogen and Phosphorus Dual-Doped Hierarchical Porous Carbon	Unknown	50	Unknown	-0.03V	[s23]
Highly Nitrogen-doped Narbon Napsules	0.657	50	-0.25V	-0.06V	[s24]

Nitrogen-doped Narbon Nanosheets	0.6	100	-0.28V	-0.01V	[s25]

Table S4. The *n* (from -0.1V to -0.3V) of different catalysts derived from the K–L equation [Eq. (S1and S2)] and RRDE curves (Eq. (S3 and S4)) (values in parentheses).

	GF	N-GF	S-GF	N-S-GF	GMF	N-GMF	S-GMF	N-S-GMF	Pt/C
-0.1V	* (1.0)	* (0.7)	* (1.0)	* (3.2)	* (0.4)	* (3.0)	* (3.2)	2.3 (3.8)	* (3.92)
-0.2V	* (2.0)	* (2.0)	* (2.48)	* (3.7)	* (1.0)	3.4 (3.2)	2.0 (3.2)	3.0 (3.88)	3.9 (3.95)
-0.3V	* (2.7)	* (2.4)	2.1 (2.9)	3.0 (3.5)	2.0 (2.8)	2.8 (3.3)	2.0 (3.0)	3.2 (3.87)	3.7 (3.96)

* Values of *n* can not be obtained from K–L equation due to the not linear K-L plots at these potentials.

References

[s1] Y. Li, Y. Zhao, H. Cheng, Y. Hu, G. Q. Shi, L. M. Dai, L. T. Qu, *J. Am. Chem. Soc.* **2012**, *134*, 15.

[s2] Y. Zhao, J. Liu,Y. Hu, H. Cheng, C. Hu, C. Jiang, L. Jiang, A. Cao, L. Qu, *Adv. Mater.* **2013**, *25*, 591.

[s3] M. Wang etc, Sci. Rep. 2013, 3 1238−1244

[s4] Han. Hu, Z. B. Zhao, W. Wan, Y. Gogotsi, J. Qiu, *Adv. Mater.* **2013**, *25*, 2219.

[s5] Y. Liu, W. Qian, Q. Zhang, A. Cao, Z. Li, W. Zhou, Y. Ma, F. Wei, *Nano Lett.* **2008**, *8*, 1323.

[s6] J. Liang, Y. Jiao, M. Jaroniec, S. Z. Qiao, *Angew. Chem. Int. Ed.* **2012**, *51*, 11496.

[s7] Y. Zheng, Y. Jiao, L. Ge, M. Jaroniec, S. Z. Qiao, *Angew. Chem. Int. Ed.* **2013**, *52*, 3110.

[s8] Z. H. Sheng, L. Shao, J. J. Chen, W. J. Bao, F. B. Wang, X. H. Xia, *ACS Nano* **2011**, *5*, 4350.

[s9] Z. Yang, Z. Yao, G. Li, G. Fang, H. Nie, Z. Liu, X. Zhou, X. Chen, S. Huang, *ACS Nano* **2012**, *6*, 205.

[s10] I. Y. Jeon, S. Zhang, L. Zhang, H. J. Choi, J. M. Seo, Z. Xia, L. M. Dai, J. B. Baek, *Adv. Mater.* **2013**, *25*, 6138.

[s11] Y. Zhao, C. Hu, Y. Hu, H. Cheng, G. Shi, L. Qu, *Angew. Chem. Int. Ed.* **2012**, *51*, 11371.

[s12] S.Yang, L. Zhi, K. Tang, X. L. Feng, J. Maier, K. Müllen, *Adv. Funct. Mater.* **2012**, *22*, 3634.

[s13] J. Xu, G. Dong, C. Jin, M. Huang, L. Guan, *ChemSusChem* **2013**, *6*, 493.

[s14] J. Liang, X. Du, C. Gibson, X. W. Du, S. Z. Qiao, *Adv. Mater.* **2013**, *25*, 6226.

[s15] Y. Zhang, J. Ge, L. Wang, D. Wang, F. Ding, X. Tao, W. Chen, *Sci. Rep.* **2013**, *3*, 2771.

[s16] H. L. Jiang, Y. Su, Y. Zhu, J. Shen, X. Yang, Q. Feng, C. Li, *J. Mater. Chem. A,* **2013**, *1*, 12074.

[s17] S. Chen, J. Bi, Y. Zhao, L. Yang, C. Zhang, Y. Ma, Q. Wu, X. Wang, Z. Hu, *Adv. Mater.* **2012**, *24*, 5593.

[s18] J. Xu, Y. Zhao, C. Shen, L. Guan, *ACS Appl. Mater. Interfaces* **2013**, *5*, 12594.

[s19] Z. Liu, H. Nie, Z. Yang, J. Zhang, Z. Jin, Y. Lu, Z. Xiao, S. Huang, *Nanoscale*, **2013**, *5*, 3283.

[s20] W. Yang, T. Fellinger, M. Antonietti, *J. Am. Chem. Soc.* **2011**, *133*, 206.

[s21] Y. Wang, X. Jiang, *ACS Appl. Mater. Interfaces* **2013**, *5*, 11597.

[s22] J. Liang, X. Du, C. Gibson, X. W. Du, S. Z. Qiao, *Adv. Mater.* **2013**, *25*, 6226.

[s23] H. Jiang, Y. Zhu, Q. Feng, Y. Su, X. Yang, C. Li *Chem. Eur. J.* DOI : 10.1002/chem.201304561.

[s24] C. Hu, Y. Xiao, Y. Zhao, N. Chen, Z. Zhang , M. Cao, L. Qu, *Nanoscale*, **2013**, *5*, 2726.

[s25] W. Wei, H. Liang, K. Parvez, X. Zhuang, X. Feng, K. Müllen, *Angew. Chem.* **2014**, *26*, 1596.